PAPER

Check for updates

Facile synthesis of Al-stabilized lithium garnets by a solution-combustion technique for all solid-state batteries†

Pavan Badami, [iD] [a] Stefan Smetaczek, [iD] [b] Andreas Limbeck, [iD] [b] Daniel Rettenwander, [iD] [cd] Candace K. Chan [iD] *[e] and Arunachala Nadar Mada Kannan [iD] *[a]

Garnet-type solid electrolytes with cubic modification (c-LLZO, $Li_7La_3Zr_2O_{12}$) are considered to be one of the most promising candidates for SSLBs with desirable properties such as high ionic conductivity (about 1 mS cm^{-1}) at room temperature, a wide electrochemical operational window, and good stability against reduction by Li metal. The synthesis and processing of garnets through conventional wet-chemical, solid-state reaction and nitrate-combustion approaches often requires one or more of the following processing conditions (energy intensive milling steps, multiple and long periods of calcination) to attain a conductive cubic phase making synthesis time intensive. Herein, we report a facile fuel-assisted solution combustion method using carbohydrazide−nitrate mixtures to synthesize cubic-$Li_{6.28}Al_{0.24}La_3Zr_2O_{12}$ (Al-LLZO); compared to other nitrate-combustion approaches, utilizing a nitrogen containing fuel source (CH_6N_4O) offers drastic reduction in the synthesis duration at relatively low temperatures. Selection of the right fuel to oxidizer ratio and annealing conditions is found to be critical for attaining phase purity and particle growth size of LLZO powders. Cubic phase Al-LLZO with a particle size of up to ∼200 nm was attained at temperatures as low as 800 °C upon calcining the as-combusted powders for 4 h. The green pellets attained high relative densities of 90−92% and ionic conductivities up to 0.45 mS cm^{-1} at low sintering conditions of 1100 °C for 6 h compared to longer sintering duration (∼10−24 h) for LLZO prepared with a common solid-state reaction or wet chemical methods using conventional pressure-less sintering methods. Sintered pellets exhibited a low activation energy of 0.29 eV likely due to the low grain boundary resistance. Synthesizing sub-micron sized Al-LLZO powders through low-cost facile synthesis approaches is of great importance in the fabrication of composite electrolytes and catholytes.

[a] *The Polytechnic School, Ira A. Fulton Schools of Engineering, Arizona State University, Mesa, AZ, 85212, USA. E-mail: amk@asu.edu*

[b] *Institute of Chemical Technologies and Analytics, TU Wien, 1060 Vienna, Austria*

[c] *Department of Material Science and Engineering, NTNU Norwegian University of Science and Technology, Trondheim, Norway*

[d] *International Christian Doppler Laboratory for Solid-State Batteries, NTNU Norwegian University of Science and Technology, Trondheim, Norway*

[e] *Materials Science and Engineering, School for Engineering of Matter, Transport and Energy, Arizona State University, Tempe, AZ, 85287, USA. E-mail: candace.chan@asu.edu*

1. Introduction

Li-ion batteries (LiBs) with organic solvent-based electrolytes suffer from flammability and show poor electrochemical compatibility with high voltage cathode materials.[1,2] They also suffer from poor rate capabilities at lower temperatures and are un-safe to operate at elevated temperatures (beyond 40 °C), while the next-generation of LiBs using Li-metal anodes and a solid electrolyte are anticipated to overcome drawbacks associated with liquid-based LiBs and can deliver up to a two-fold increase in energy density.[3] A robust ceramic solid electrolyte with ionic conductivity above 1 mS cm^{-1} at room temperature with excellent chemical and mechanical properties is expected to inhibit dendritic growth causing short circuits, playing a key role in the development of solid-state Li batteries (SSLBs).[3,4] Among numerous solid Li$^+$ ion conductors, the Li-stuffed garnet-type oxide ($Li_7La_3Zr_2O_{12}$ (LLZO))[5] has gained much attention as a

potential solid electrolyte for SSLBs owing to its high ionic conductivity at room temperature and good electrochemical stability against metallic Li anodes.[6] While LLZO exhibits two polymorphs *i.e.* cubic (c-LLZO, $Ia\bar{3}d$) and tetragonal (t-LLZO, $I4_1/acd$) phases,[7] the latter shows two orders of magnitude lower ionic conductivity compared to the cubic phase. c-LLZO is stabilized at room temperature by aliovalent doping of metal cations either at the Li^+ sites using Al^{3+},[8] Ga^{3+}[9] or the Zr^{4+} sites with Ta^{5+}[10] or Nb^{5+}[11] to overcome formation of thermodynamically favorable t-LLZO. Among all the doped derivatives, Al-doped LLZO still remains an attractive candidate due to its good sinterability and cost competitiveness.[12–14]

LLZO is a conventionally synthesized using solid-state reaction (SSR), which often requires time-intensive milling periods of precursors and high reaction temperatures (>1200 °C) to attain a conductive cubic phase.[15] Moreover, the high temperature synthesis route generally produces micron-sized particles with large aggregates, making it difficult for processing dense pellets and composite electrode–electrolyte assembly. Even though wet chemical routes like sol–gel,[16,17] Pechini,[18] co-precipitation,[19] and spray pyrolysis[20,21] share the advantage of producing fine particles of LLZO at lower temperatures (<900 °C), these synthesis methods require the use of either expensive precursors, multiple drying/calcination steps to remove water and organic solvents *etc.* along with long durations of annealing to attain phase pure conductive c-LLZO making the process elaborate. For example, Sakomoto *et al.*[22] synthesized cubic Al-LLZO ~ 900 °C using a low temperature sol–gel synthesis route, however it required long intermediate drying steps along with a supercritical fluid extraction step to retain nano-scale features. In another study,[23] Al-doped LLZO was synthesized using a nitrate-combustion method, but the desired cubic phase (without secondary phases) was attained only at elevated reaction temperatures (>950 °C). Several studies report low-temperature synthesis of Al-doped LLZO below 850 °C,[24–29] but the calcined powders lacked phase purity or the as-synthesized powders required additional milling steps, or long duration sintering (>10 h) to attain dense and conductive pellets. Therefore, producing submicron LLZO powders through less process intensive and low processing temperatures is of importance to prepare dense pellets under low sintering conditions and allow stable interface contact between LLZO/cathodes to build SSLBs.[30–33] In addition, nano-sized LLZO powders are of great importance as they act as active fillers to improve Li^+ transport and mechanical properties of solid polymer electrolytes such as poly(ethylene oxide) or polyacrylonitrile (PAN).[34,35]

Herein, an alternative facile fuel assisted wet-chemical route (solution combustion synthesis – SCS) is adopted to synthesize Al-LLZO having nominal composition $Li_{6.28}Al_{0.24}La_3Zr_2O_{12}$;[36] eliminating intermediate drying steps of precursors and long duration annealing steps involved in the wet-chemical and solid-state reaction method. SCS is an attractive method for synthesizing high purity nano-sized functional materials using inexpensive precursors and fuel, wherein the oxidizers and fuels undergo self-sustained and fast redox reactions under the influence of an external heat source.[37,38] Here, we achieve sub-micron sized cubic Al- LLZO powders at low reaction temperatures 800 °C in 4 h with optimized processing conditions (*i.e.* fuel ratio, calcination duration). The Al-LLZO pellets attained a relative density of $\sim 92\%$ with Li^+ conductivities up to 0.45 mS cm^{-1} at room temperature through a conventional sintering method.

2. Experimental section

2.1 Synthesis and pelletization of Al-LLZO

$Li_{6.28}Al_{0.24}La_3Zr_2O_{12}$ (Al-LLZO) was synthesized as described in the flowchart given in Fig. 1. Stoichiometric amounts of $LiNO_3$ (Alfa Aesar, CAS No. 7790-69-4, 10 wt% excess Li source was added to compensate Li loss during the combustion reaction or sintering), $La(NO_3)_3 \cdot 6H_2O$ (Alfa Aesar, CAS No. 10277-43-7), $Al(NO_3)_3 \cdot 9H_2O$ (Millipore Sigma, CAS No. 7784-27-2) and $ZrO(NO_3) \cdot xH_2O$ (Millipore Sigma, CAS No. 14985-18-3) were dissolved in a minimum amount of ultra-pure DI water at 80 °C. Later, carbohydrazide (CH_6N_4O) fuel (Millipore Sigma, CAS No. 497-18-7) was dissolved in ultra-pure DI water and subsequently mixed/stirred with the precursor solution at 80 °C for about 10 min until gelation occurred. The molar concentration of the fuel was determined based on the total oxidizing and reducing valences as described by Jain *et al.*[39] and the detailed calculations are provided in the ESI.† The dehydrated gel was introduced into a preheated muffle furnace at 500 °C to trigger combustion and the self-sustained ignition led to voluminous fine foamy product. The as-burnt foamy powder was collected, lightly ground and calcined in a MgO crucible (Tateho Ozark Technical Ceramics) between 600 and 900 °C until cubic phase Al-LLZO was obtained. The Al-LLZO green pellets were consolidated *via*
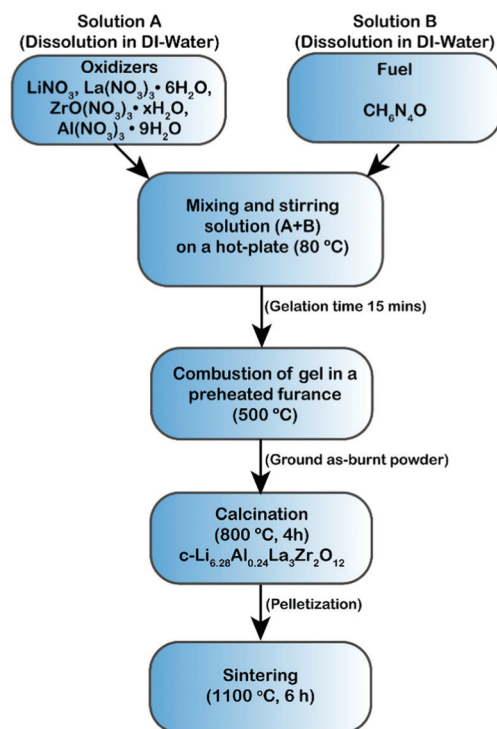

Fig. 1 Schematic representation of the combustion synthesis process for Al-LLZO.

cold-pressing using a 9 mm diameter die set at 3-ton load for 5 min. The green pellets were kept covered with the sacrificial mother powder (to prevent loss of Li) in the MgO crucible with a lid covering during sintering. The pellets were held first at 950 °C for 1 h to remove any contamination layers such as LiOH or Li_2CO_3, followed by sintering between 1000 °C and 1100 °C for 6 h. The theoretical density of the Al-LLZO pellet was considered to be 5.1 g cm^{-3} [29,53] and the relative density of the sintered pellets was calculated based on the volume and weight after sintering.

2.2 Characterization

2.2.1 Materials characterization. X-ray diffraction (XRD) was conducted for the powder and pellet samples using a Bruker D8 ADVANCE diffractometer (Ni filtered Cu radiation with wavelength $\lambda_{K\alpha 1}$ = 1.54 Å, 40 kV/50 mA) from 10 to 60° (2θ) at 5° min^{-1} in 0.02° increments. The phase detection of the crystal structure and refinements were carried out using High Score Plus. The surface morphology of the LLZO samples was examined using a FE-SEM Hitachi S-4700 operated at 15 kV and 10 µA emission current. High-angle annular dark-field (HAADF) images were recorded using a JEOL ARM 200 Scanning Transmission Electron Microscope (STEM) at 200 kV. Energy dispersive X-ray (EDS) elemental mapping was acquired with an AZtec 100 mm^2 windowless detector from Oxford Instruments. The Al-LLZO powder samples were sonicated for 10 min in methanol and the suspended particles were drop cast on a lacey-carbon grid. The surface morphology and elemental mapping of the fractured pellets were analyzed using a SEM Electron Microprobe Analyzer (JEOL JAX-8530F) operated at 15 kV and 50 nA emission current. Thermogravimetric/differential thermal analysis was carried out using a Labsys Evo in air up to 900 °C at 5 °C min^{-1}.

2.2.2 Inductively coupled plasma optical emission spectroscopy. Compositional analysis of the Al-LLZO samples was performed using inductively coupled plasma optical emission spectroscopy (ICP-OES). An iCAP 6500 RAD (Thermo Fisher Scientific, USA) and Qtegra software provided by the manufacturer of the instrument was used for all measurements. Detailed information about the used instrumental settings is shown in Table S2 (ESI†). For sample digestion, borax fusion was used: 50 mg samples (crushed and ground using an agate mortar to ensure homogeneity) were mixed with 0.8 g borax and heated to 1000 °C for 5 h. A HCl/HF/H_2O mixture (10 m% HCl, 0.8 m% HF) at 70 °C was used to dissolve the solidified fusions. For signal quantification, conventional external calibration using aqueous standards prepared from certified single element ICP-standard solutions was used. Internal standardization (0.2 mg kg^{-1} europium) was applied to correct instrumental drifts and variations in sample introduction.

2.2.3 Electrochemical impedance spectroscopy. The sintered LLZO pellets were polished using SiC paper (800, 1000 and 1200 grit sizes) to obtain a mirror finish surface followed by gold sputtering (thickness 100 nm). Impedance measurements were carried out from 0 to 60 °C with 20 °C steps using a Biologic SP-200 Potentiostat/Galvanostat/FRA from 7 MHz to 10 mHz to estimate conductivity and activation energy. Impedance spectra analysis

was carried out using ZView software. Prior to each impedance measurement, the pellets were stabilized at the set temperature for ~30 min.

3. Results and discussion

3.1 Effect of fuel to oxidizer ratio on morphology, phase purity and formation mechanism

The exothermic nature of the combustion reaction is governed by the type of fuel and fuel to oxidizer ratio (F/O), which in-turn defines the microstructure, crystallinity, and phase purity of the combusted product.[40] In the present study, a water-soluble fuel *i.e.*, carbohydrazide (CH_6N_4O) having a low melting point: ~154 °C was utilized for synthesizing Al-substituted LLZO. Previously, carbohydrazide based fuels have been utilized to synthesize various high purity nanostructured ceramics and spinel aluminates.[41,42] In addition, hydrazine-based fuels act as a chelator forming bidentate ligands with metal cations to prevent selective precipitation on dehydration of water promoting homogenous combustion.[43–45] To understand the formation mechanism of cubic Al-LLZO, the F/O ratio was systematically varied from a fuel-lean zone (F/O = 0.5) to fuel-rich zone (F/O = 4.0), followed by a calcination step of as-burnt powders at 900 °C for a duration of 4 h (see Table S3, ESI† for the nature of the combustion). The calcined powder samples were characterized by XRD and SEM for optimizing the molar concentration of the fuel to control phase purity and morphology of the Al-LLZO powders.

The XRD patterns (see Fig. 2) of calcined powders showed reflections from the cubic phase of Al-LLZO for all values of F/O ratios on calcining at 900 °C for 4 h with varied intensity of flame on combustion. In general, fuel lean conditions (F/O = <1) produce sluggish combustion reactions, while fuel rich conditions (F/O = >1) produce smolder type reactions. Whereas stoichiometric fuel conditions (F/O = 1) led to high intensity flame type reactions following a similar trend observed elsewhere.[46] On calcining the as-burnt powders, the presence of a minor intermediate phase of $Li_{0.5}La_2Al_{0.5}O_4$ (JCPD 04-1167) was observed for F/O ratios between 0.5 and 2, in addition to cubic Al-LLZO as a
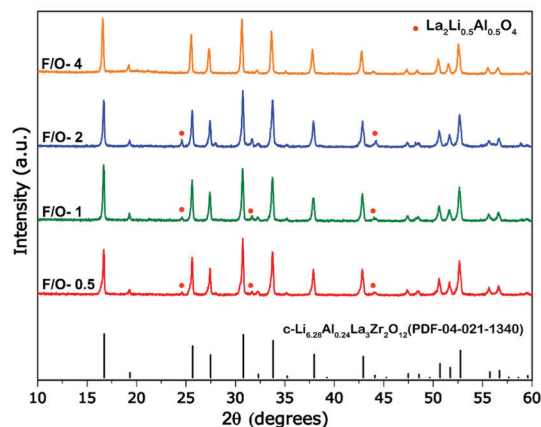

Fig. 2 XRD patterns of calcined Al-LLZO samples with various fuel to oxidizer (F/O) ratios.

major phase. The formation of $Li_{0.5}La_2Al_{0.5}O_4$ as an intermediate phase is commonly observed with both high temperature synthesis routes and wet synthesis routes due to the reaction between $LaAlO_3$ and excess Li source which forms at sufficiently low temperatures ($\sim 600\ ^{\circ}C$) compared to the conductive cubic-LLZO phase.[18,47] However, increasing the F/O value to 4 led to complete transformation of precursors to the cubic phase without any intermediated or impurity phases such as $Li_{0.5}La_2Al_{0.5}O_4$, $La_2Zr_2O_7$, $LaAlO_3$ and γ-Al_2O_3, which are common in the case of solid-state reaction methods.[8,48] Absence of impurity phases can be attributed to high enthalpy and flame temperatures caused by increasing molar concentration of the fuel.[49]

Fig. 3(a–h) shows the representative scanning electron micrographs of Al-LLZO powders with varying F/O ratios. At an F/O ratio of 0.5 (*i.e.*, fuel-lean condition), the Al-LLZO sample showed mixed morphologies of spherical shape (0.5 to 1.0 μm) and ligamentous structures as observed in Fig. 3a and b. Increasing the F/O ratio value to 1 (*i.e.*, stoichiometric conditions) led to growth in the particle size with a reduction in the porosity, and the morphology exhibited well-sintered ligamental type growth (Fig. 3c and d). Under the fuel-rich conditions (F/O = 2, 4), the particle morphology observed was predominantly near

uniform ligament structures having a width of ~ 2 μm with limited porosity (Fig. 3(e)–(h)). In general, lower F/O ratios produce near spherical particles, preventing necking and growth in the particle sizes due to lower enthalpy of the reactions, while the higher F/O ratios cause interparticle grain growth with an increase in the combustion flame temperatures and limited CO_2 and NO_2 evolution.[46,50]

On setting the F/O ratio to 4, calcination temperatures were optimized between 600 and 900 $^{\circ}C$ to attain a cubic Al-LLZO phase. The XRD pattern for the Al-LLZO sample before calcination revealed the presence of a nanocrystalline $La_2Zr_2O_7$ pyrochlore phase (Fig. 4a), which is observed with sol–gel[22] and other synthesis methods.[16,21] STEM and EDS mapping analysis carried out on the as-burnt powder confirmed homogenous distribution of the Al dopant (Fig. 4b) eliminating the possibility of forming unfavorable, less conductive t-LLZO or mixed c-LLZO/t-LLZO phases. By calcining the as-burnt powder above 600 $^{\circ}C$ for 4 h, formation of a c-LLZO phase was observed (Fig. 4a) along with minor phases of $Li_{0.5}La_2Al_{0.5}O_4$ up to 700 $^{\circ}C$. However, calcination at 800 $^{\circ}C$ led to complete formation of c-LLZO without any intermediate phases with a lattice constant of 12.98 Å (see Table S4, ESI†), which agrees with that by the solid-state reaction methods.[57] The calcined powders at 800 $^{\circ}C$ showed a particle size of approximately 200 nm with homogenous distribution of Al along the grains as seen in Fig. 4c. ICP-OES analysis of the Al-LLZO powder calcined at 800 $^{\circ}C$ revealed powder with the composition $Li_{6.58}Al_{0.22}La_{2.91}Zr_2O_{12}$ (refer to Table S4, ESI†) which is very near to the targeted synthesis composition.

The TGA-DTA analysis of the as-burnt powder with an F/O ratio of 4.0 was carried out to evaluate the thermal decomposition process up to 900 $^{\circ}C$, as shown in Fig. 4d. During the heating process from RT up to 50 $^{\circ}C$, a slight increase in mass was observed (region 1) under the TG curve, possibly due to uptake of moisture from the air. Followed by the presence of a weak exothermic peak around 130 $^{\circ}C$ with a weight loss of *ca.* 6% associated to the loss of a water molecule (as seen in region 1 of Fig. 4d). Furthermore, a sharp endothermic peak observed at 250 $^{\circ}C$ (region 2) can be assigned due to decomposition of residual nitrates and decomposition of the fuel liberating CO_2.[51] The presence of a weak exothermic peak observed at 450 $^{\circ}C$ is unknown, as $La_2Zr_2O_7$ crystallizes beyond 700 $^{\circ}C$.[52] Significant weight loss is observed in region 3 between 500 and 650 $^{\circ}C$ with the onset of an endothermic peak at around 600 $^{\circ}C$ suggesting growth of the LLZO phase. Above 650 $^{\circ}C$, there is no significant weight loss or endo/exothermic peaks observed indicating the formation of a well-stabilized cubic Al-LLZO phase.

3.2 Effect of sintering temperatures on microstructure and ionic conductivity

The Al-LLZO powders calcined at 800 $^{\circ}C$ for 4 h were selected for fabricating green pellets followed by sintering between 900 and 1200 $^{\circ}C$ for 6 h to evaluate the microstructural and Li$^+$ transport properties. The sintering duration of 6 h was selected throughout the experiments to avoid excess Li loss from the garnets. The pellets sintered at 900 $^{\circ}C$ for 6 h exhibited a low relative density of only $\sim 75\%$, featuring large open pores with
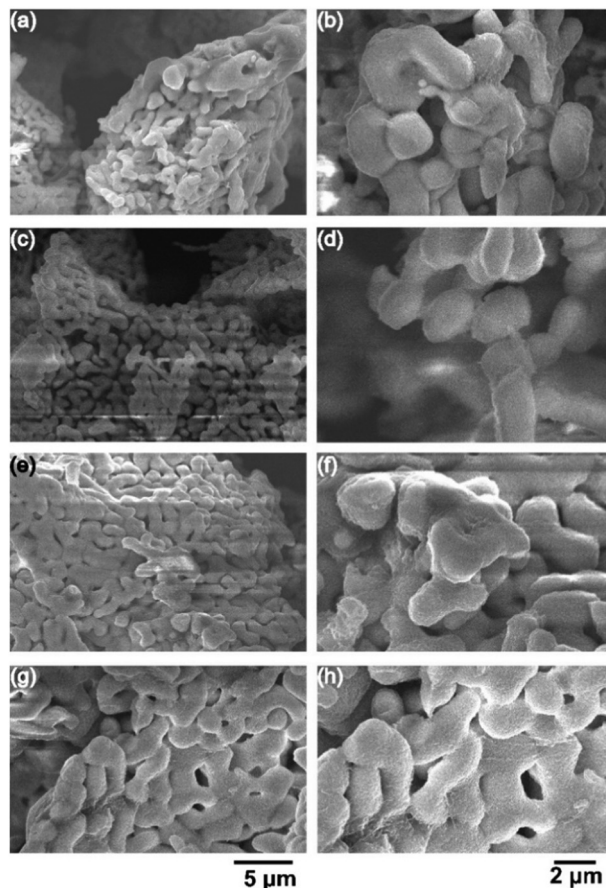

Fig. 3 Representative SEM images of Al–LLZO powders synthesized by a combustion method with various fuel to oxidizer (F/O) ratios of (a and b) 0.5, (c and d) 1.0, (e and f) 2.0 and (g and h) 4.0 at two different magnifications.
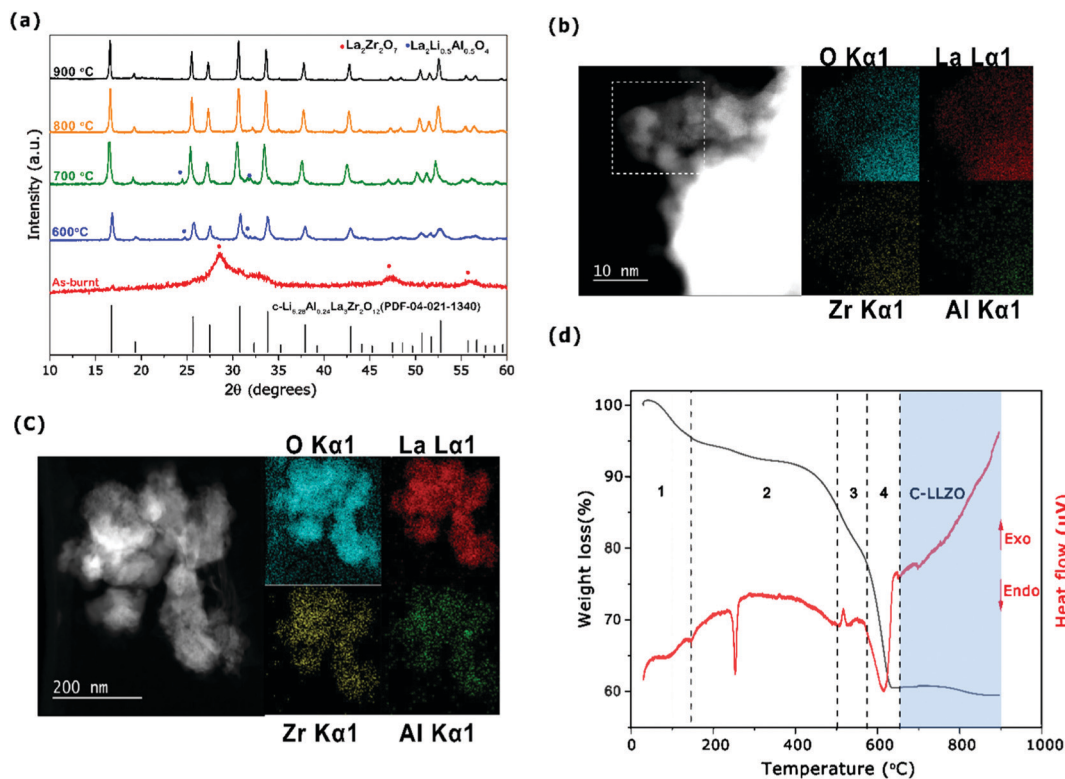
Fig. 4 (a) XRD patterns of Al-LLZO synthesized with an F/O ratio of 4.0 calcined between 600 and 900 °C for 4 h. (b) STEM-EDS elemental map of as-combusted powders showing elemental distribution for O, La, Zr, and Al. (c) STEM-EDS elemental mapping of Al-LLZO calcined at 800 °C for 4 h along the grains. (d) TGA-DTA analysis of the as-combusted powders from room temperature until crystallization of the c-LLZO phase (up to 900 °C).

intergranular fractures (see Fig. 5a). Incomplete densification of pellet led to poor Li$^+$ conductivity (as seen in the Nyquist plot, Fig. S1, ESI†). Sintering pellets at 1000 °C for 6 h led to the increase in relative density reaching up to ~86% and improved

Li$^+$ ionic conductivity to 0.2 mS cm^{-1}. However, fractured SEM images of the pellets showed the presence of uniformly distributed pores, as seen in Fig. 5b. The presence of open pores seen in Fig. 5b is likely caused by liquid phase sintering of a
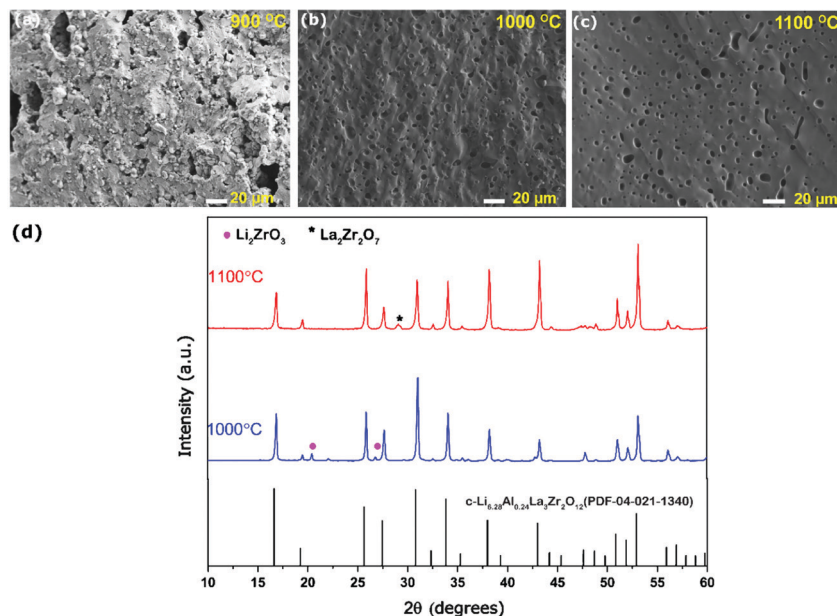

Fig. 5 SEM fractured surface images of Al-LLZO pellets sintered at (a) 900 °C, (b) 1000 °C, and (c) 1100 °C, and (d) XRD patterns of the conductive pellets sintered at 1000 °C and 1100 °C for 6 h (c-Li$_{6.28}$Al$_{0.24}$La$_3$Zr$_2$O$_{12}$ phase # PDF: 04-021-1340, Li$_2$ZrO$_3$ phase PDF # 016-0263 and La$_2$Zr$_2$O$_7$ phase # 01-070-5602).

Li–Al–O eutectic mixture, which occurs at ∼1055 °C leading to partial or incomplete accelerated grain growth leaving behind pores.[32,55] The XRD scan of the sintered pellet revealed cubic Al-LLZO as a major phase along with minor traces of Li_2ZrO_3. Li_2ZrO_3 is commonly reported during the sintering of Al-LLZO, which is formed as an intermediate phase due to reaction between excess Li and Zr source in the garnet or in some cases observed as a surface contamination on exposure to air and found to disappear during polishing of the pellet surface.[32,47,53] On ramping up the sintering temperature to 1100 °C, the pellets retained c-LLZO as the main phase showing a high relative density of 92% and high Li^+ conductivity of 0.45 mS cm^{-1}. The fractured surface SEM image (in Fig. 5c) showed a flat surface indicating transgranular fracture with high grain boundary strength and limited pores compared to pellets sintered at 1000 °C for 6 h. The presence of tiny closed pores can be attributed to several factors such as Li_2O loss during the sintering process or due to smaller particles of as-synthesized powders, which may prevent full densification caused by poor necking.[32,53,54] Interestingly, pellets sintered at 1100 °C did not exhibit Li_2ZrO_3 minor phases (Fig. 5d) in the absence of excess Li source and also no Al-rich secondary phases such as $LaAlO_3$ were observed leading to resistive grain-boundary transport.[55] A minor peak of $La_2Zr_2O_7$ was detected at $2\theta \sim 29°$ on the surface of the pellet but did not show any severe impact on the Li^+ ion conductivity. The ICP-OES analysis confirmed a slight loss in the Li content of pellets sintered at 1100 °C ($Li_{6.24}Al_{0.20}La_{2.89}Zr_2O_{11.8}$, refer to Table S5, ESI†) compared to the starting composition of the powder ($Li_{6.58}Al_{0.22}La_{2.91}Zr_2O_{12}$). However, Li and Al mole concentration of the pellet was found to be in the optimum stoichiometric range to form the fast conductive cubic Al-LLZO phase preventing formation of the t-LLZO phase caused by either excess Li concentration (>6.24 moles) or low Al concentration (<0.20 moles).[36] EDS mapping carried out on the cross-section of the pellets confirms no presence of Al-rich phases at the grain boundaries (Fig. S1, ESI†). Pellets sintered at 1200 °C/6 h, showed a prominent non-conductive $La_2Zr_2O_7$ pyrochlore phase (Fig. S2, ESI†) causing a drop in Li-ion conductivity below <0.1 mS cm^{-1}, but had superior theoretical density up to 95% as the $La_2Zr_2O_7$ (6.04 g cm^{-3}) phase has a high density compared to the cubic Al-LLZO phase (5.10 g cm^{-3}).

The complex plane impedance patterns of the Al-LLZO pellets sintered under optimal conditions (1100 °C, 6 h) recorded from 0 to 60 °C are shown in Fig. 6a. At lower temperatures (0 and 20 °C), the impedance spectra show a high-frequency arc representing a resistor connected in parallel to a constant phase element ($R||CPE$), followed by a strong increase of the imaginary part of the complex impedance towards lower frequencies which is attributed to the ideal ionically blocking electrodes represented by $R_e||CPE_e$ connected in series. In general, the total ionic conductivity in a ceramic conductor is a function of both bulk and grain boundary contributions represented by distinctive high and mid frequency arcs.[56] Based on the capacitance value, $C_i = (R^{1-n}CPE_i)^{1/n}$, where n is a fitting parameter describing deviation from the ideal that is Debye response ($n = 1$), the high frequency
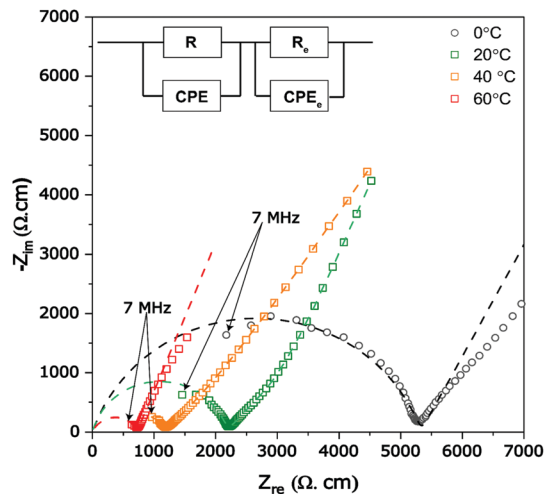

Fig. 6 Complex plane temperature-dependent impedance plots (symbols) measured from (0 to 60 °C) of sintered Al-LLZO pellets along the fitted equivalent circuit (dotted lines).

Table 1 Equivalent circuit fit parameters and corresponding total conductivity values at various temperatures

Temperatures (°C)	ρ (Ω cm)	$C_{b,gb(=total)}$ (nF)	$n_{b=total}$	σ_{total} (mS cm^{-1})
0	5215	3.23	0.80	0.2
20	2147	2.2	0.80	0.45
40	1150	0.11	0.73	0.86
60	682	0.10	0.72	1.46

arc is assigned to grain boundary processes indicating that the long-range Li^+ transport is dominated by grain boundaries (see Table 1).

As seen in Fig. 6a, the arcs shift towards higher frequencies with increasing temperature according to $\omega = 1/RC$, where ω is the resonance frequency, due to decreasing resistance. The temperature dependence of total Li^+ conductivity ($\sigma_{total} = \sigma_{gb}$) of Al-LLZO pellets sintered at 1100 °C recorded between 0–60 °C is shown using an Arrhenius plot in Fig. S4 (ESI†). The activation energy E_a for the linear behavior was calculated using $\sigma_{total}T = \sigma_0 \exp(-E_a/(k_BT))$, where k_B is Boltzmann's constant and σ_0 the pre-factor. The activation energy of the Al-LLZO pellet prepared by a solution-combustion method was found 0.29 eV, which is lower compared to that by the solid-state reaction method and comparable to samples prepared by wet-chemical routes (refer to Table 2). Low values of the activation energy (calculated in the given temperature range) could be attributed to the superior grain boundary contacts and excellent sinterability of Al-LLZO powders prepared by a solution combustion route.[17,21]

Table 2 contains a comparison of the relative density, Li^+ conductivity and activation energy for Al-doped LLZO pellets prepared by various methods in the literature along with the present method. Evidently, carbohydrazide–nitrate solution-combustion is a facile method with a third of the duration necessitated by the solid-state reaction method and eliminates elaborated processes like multiple calcination/drying steps involved with the wet chemical routes. The pellet densification

Table 2 Comparison of synthesis/sintering conditions and properties of the Al-LLZO prepared by a solution-combustion method in the literature

Synthesis conditions				Sintering conditions			Pellet properties			
Synthesis route Al-LLZO	Processing conditions	Temperature (°C)	Duration (h)	Temperature (°C)	Duration (h)	Crucible/technique	Relative density (%)	σ_{total} (mS cm^{-1})	E_a (eV)	Ref.
Solid-state[a]	Milling (16 h)	900	10	1230	6	Alumina/conventional	90	0.18	0.41	13
Solid-state[a]	Milling (0.5 h)	1000	12	1100	6 or 12	Alumina/conventional	94	0.5	0.29	32
Solid-state[a]	Milling (9 h)	600, 800	12, 12	850	40	NA/conventional	NA	0.14	0.33	25
Modified solid-state	Milling (2 h)/ ultrasonication	70, 100, 200, 750	2, 0.5, 1, 3	1100	3	NA/conventional	91	0.16	0.36	29
Solid-state[a]	Milling (12 h)	900	12	1200	24	Pt/conventional	96	0.44	0.37	57
Hybrid sol-gel[b]		550-600, 900[d]	NA, 1	1100	3	NA/microwave hybrid furnace	NA	0.3	0.28	17
Pechini		900	6	1200	6	Alumina/conventional	NA	0.2	NA	18
Pechini[c]		700	2	600	30 (s)	Reactive flash sintering	93	0.18	0.24	24
Sol–gel[c]	Gel drying (48 h)	450, 600	4, 4	1000		Hot-press (40 MPa)	96	0.4	0.26	22
Co-precipitation	Gel ageing (12 h)	600–900	6	1000	0.16	Field assisted sintering	96	0.33	0.32	58
Molten salt		900	4	1100	18	MgO/conventional	84	0.23	NA	59
Glycine-combustion		950	24	1200	24	Alumina/conventional	95	0.5	0.29	23
Carbohydrazide-combustion		800	4	1100	6	MgO/conventional	92	0.45	0.29	This work
				1000			86	0.2		
				900			75			

[a] Involves multiple milling steps (before and after calcination step). [b] Needs additional synthesis step to prepare amorphous aluminum oxide for incorporation. [c] As-synthesized powders showed impurity phases ($La_2Zr_2O_7$, $Li_{0.5}Al_{0.5}La_2O_4$). [d] Pre-calcination step to initiate garnet phase. NA = Not available.

is also faster without any milling or long sintering durations (>10 h) (see Table 2 for comparisons).

4. Conclusions

In summary, submicron sized cubic $Li_{6.28}Al_{0.24}La_3Zr_2O_{12}$ (Al-LLZO) was synthesized by a solution-combustion method using carbohydrazide–nitrate mixtures. The presented synthesis route eliminates long ageing/drying steps, multiple calcination steps usually involved with the wet-chemical route, producing cubic Al-LLZO powders through a single low-temperature calcination step (800 °C, 4 h). The synthesis parameters such as the fuel to oxidizer ratio, and calcination temperatures were studied and optimized to produce single-phase cubic Al-LLZO powders without any intermediated phases. The pellets sintered at 1100 °C for 6 h with 92% relative density exhibited Li^+ conductivity up to 0.45 mS cm^{-1} at room temperature. The Al-LLZO pellets sintered at 1100 °C showed activation energies of 0.29 eV in the temperature range between 0 and 60 °C, which were lower compared to those prepared by the solid-state reaction method (0.37 eV) or similar to the values attained by wet-chemical routes. Evidently, the carbohydrazide–nitrate based solution-combustion can be a potential viable method for commercially producing Al-LLZO powders at low temperatures, utilizing inexpensive precursors and less time intensive processing conditions. In addition, access to submicron sized powders using a facile route would provide opportunities for preparing composite high voltage cathodes through co-sintering at lower temperatures and could be used as a low-cost nanoscale LLZO filler for polymer–ceramic composite membranes.

Conflicts of interest

There are no conflicts to declare.

Acknowledgements

References

1 F. Zheng, M. Kotobuki, S. Song, M. O. Lai and L. Lu, *J. Power Sources*, 2018, **389**, 198–213.

2 S. Chen, K. Wen, J. Fan, Y. Bando and D. Golberg, *J. Mater. Chem. A*, 2018, **6**, 11631–11663.

3 H. Liu, X. B. Cheng, J. Q. Huang, H. Yuan, Y. Lu, C. Yan, G. L. Zhu, R. Xu, C. Z. Zhao, L. P. Hou, C. He, S. Kaskel and Q. Zhang, *ACS Energy Lett.*, 2020, **5**, 833–843.

4 P. Knauth, *Solid State Ionics*, 2009, **180**, 911–916.

5 R. Murugan, V. Thangadurai and W. Weppner, *Angew. Chem., Int. Ed.*, 2007, **46**, 7778–7781.

6 V. Thangadurai, S. Narayanan and D. Pinzaru, *Chem. Soc. Rev.*, 2014, **43**, 4714–4727.

7 J. Awaka, N. Kijima, H. Hayakawa and J. Akimoto, *J. Solid State Chem.*, 2009, **182**, 2046–2052.

8 A. Düvel, A. Kuhn, L. Robben, M. Wilkening and P. Heitjans, *J. Phys. Chem. C*, 2012, **116**, 15192–15202.

9 D. Rettenwander, C. A. Geiger, M. Tribus, P. Tropper and G. Amthauer, *Inorg. Chem.*, 2014, **53**, 6264–6269.

10 Y. Li, J. T. Han, C. A. Wang, H. Xie and J. B. Goodenough, *J. Mater. Chem.*, 2012, **22**, 15357–15361.

11 C. Liu, K. Rui, C. Shen, M. E. Badding, G. Zhang and Z. Wen, *J. Power Sources*, 2015, **282**, 286–293.

12 X. Huang, Y. Lu, Z. Song, K. Rui, Q. Wang, T. Xiu, M. E. Badding and Z. Wen, *Energy Storage Mater.*, 2019, **22**, 207–217.

13 C. Chen, Y. Sun, L. He, M. Kotobuki, E. Hanc, Y. Chen, K. Zeng and L. Lu, *ACS Appl. Energy Mater.*, 2020, **3**, 4708–4719.

14 J. Schnell, F. Tietz, C. Singer, A. Hofer, N. Billot and G. Reinhart, *Energy Environ. Sci.*, 2019, **12**, 1818–1833.

15 S. Ramakumar, C. Deviannapoorani, L. Dhivya, L. S. Shankar and R. Murugan, *Prog. Mater. Sci.*, 2017, **88**, 325–341.

16 N. Janani, S. Ramakumar, L. Dhivya, C. Deviannapoorani, K. Saranya and R. Murugan, *Ionics*, 2011, **17**, 575–580.

17 H. El-Shinawi, G. W. Paterson, D. A. MacLaren, E. J. Cussen and S. A. Corr, *J. Mater. Chem. A*, 2017, **5**, 319–329.

18 Y. Jin and P. J. McGinn, *J. Power Sources*, 2013, **239**, 326–331.

19 K. W. Kim, S. H. Yang, M. Y. Kim, M. S. Lee, J. Lim, D. R. Chang and H. S. Kim, *J. Ind. Eng. Chem.*, 2016, **36**, 279–283.

20 R. Djenadic, M. Botros, C. Benel, O. Clemens, S. Indris, A. Choudhary, T. Bergfeldt and H. Hahn, *Solid State Ionics*, 2014, **263**, 49–56.

21 E. Yi, W. Wang, J. Kieffer and R. M. Laine, *J. Mater. Chem. A*, 2016, **4**, 12947–12954.

22 J. Sakamoto, E. Rangasamy, H. Kim, Y. Kim and J. Wolfenstine, *Nanotechnology*, 2013, **24**, 1–9.

23 L. Dhivya, K. Karthik, S. Ramakumar and R. Murugan, *RSC Adv.*, 2015, **5**, 96042–96051.

24 V. Avila, B. Yoon, S. Ghose, R. Raj and L. M. Jesus, *J. Eur. Ceram. Soc.*, 2021, **41**, 2–7.

25 J. Han and J. C. Kim, *Chem. Commun.*, 2020, **56**, 15197–15200.

26 R. Mahbub, K. Huang, Z. Jensen, Z. D. Hood, J. L. M. Rupp and E. A. Olivetti, *Electrochem. Commun.*, 2020, **121**, 106860.

27 H. Xie, Y. Li and J. B. Goodenough, *Mater. Res. Bull.*, 2012, **47**, 1229–1232.

28 S. Toda, K. Ishiguro, Y. Shimonishi, A. Hirano, Y. Takeda, O. Yamamoto and N. Imanishi, *Solid State Ionics*, 2013, **233**, 102–106.

29 P. J. Kumar, K. Nishimura, M. Senna, A. Düvel, P. Heitjans, T. Kawaguchi, N. Sakamoto, N. Wakiya and H. Suzuki, *RSC Adv.*, 2016, **6**, 62656–62667.

30 G. Vardar, W. J. Bowman, Q. Lu, J. Wang, R. J. Chater, A. Aguadero, R. Seibert, J. Terry, A. Hunt, I. Waluyo, D. D. Fong, A. Jarry, E. J. Crumlin, S. L. Hellstrom, Y. M. Chiang and B. Yildiz, *Chem. Mater.*, 2018, **30**, 6259–6276.

31 E. Yi, H. Shen, S. Heywood, J. Alvarado, D. Y. Parkinson, G. Chen, S. W. Sofie and M. M. Doeff, *ACS Appl. Energy Mater.*, 2020, **3**, 170–175.

32 L. Cheng, J. S. Park, H. Hou, V. Zorba, G. Chen, T. Richardson, J. Cabana, R. Russo and M. Doeff, *J. Mater. Chem. A*, 2014, **2**, 172–181.

33 K. H. Kim, Y. Iriyama, K. Yamamoto, S. Kumazaki, T. Asaka, K. Tanabe, C. A. J. Fisher, T. Hirayama, R. Murugan and Z. Ogumi, *J. Power Sources*, 2011, **196**, 764–767.

34 Y. Sun, X. Zhan, J. Hu, Y. Wang, S. Gao, Y. Shen and Y. T. Cheng, *ACS Appl. Mater. Interfaces*, 2019, **11**, 12467–12475.

35 T. Yang, Z. D. Gordon, Y. Li and C. K. Chan, *J. Phys. Chem. C*, 2015, **119**, 14947–14953.

36 E. Rangasamy, J. Wolfenstine and J. Sakamoto, *Solid State Ionics*, 2012, **206**, 28–32.

37 W. Wen and J. Wu, *RSC Adv.*, 2014, 58090–58100.

38 K. C. Patil, S. T. Aruna and T. Mimani, *Curr. Opin. Solid State Mater. Sci.*, 2002, **6**, 507–512.

39 S. R. Jain, K. C. Adiga and V. R. Pai Verneker, *Combust. Flame*, 1981, **40**, 71–79.

40 F. T. Li, J. Ran, M. Jaroniec and S. Z. Qiao, *Nanoscale*, 2015, **7**, 17590–17610.

41 S. T. Aruna and K. C. Patil, *Nanostruct. Mater.*, 1998, **10**, 955–964.

42 T. Mimani, *J. Alloys Compd.*, 2001, **315**, 123–128.

43 G. R. Rao, B. G. Mishra and H. R. Sahu, *Mater. Lett.*, 2004, **58**, 3523–3527.

44 S. L. González-Cortés and F. E. Imbert, *Appl. Catal., A*, 2013, **452**, 117–131.

45 A. Sutka and G. Mezinskis, *Front. Mater. Sci.*, 2012, **6**, 128–141.

46 A. B. Salunkhe, V. M. Khot, M. R. Phadatare and S. H. Pawar, *J. Alloys Compd.*, 2012, **514**, 91–96.

47 Y. Chen, E. Rangasamy, C. R. Dela Cruz, C. Liang and K. An, *J. Mater. Chem. A*, 2015, **3**, 22868–22876.

48 R. D. Schmidt and J. Sakamoto, *J. Power Sources*, 2016, **324**, 126–133.

49 B. J. Hwang, R. Santhanam and D. G. Liu, *J. Power Sources*, 2001, **101**, 86–89.

50 N. M. Deraz, *J. Anal. Appl. Pyrolysis*, 2010, **88**, 103–109.

51 G. Larraz, A. Orera and M. L. Sanjuán, *J. Mater. Chem. A*, 2013, **1**, 11419–11428.

52 S. T. Aruna, C. Sanjeeviraja, N. Balaji and N. T. Manikandanath, *Surf. Coat. Technol.*, 2013, **219**, 131–138.

53 E. Yi, W. Wang, J. Kieffer and R. M. Laine, *J. Power Sources*, 2017, **352**, 156–164.

54 L. Cheng, W. Chen, M. Kunz, K. Persson, N. Tamura, G. Chen and M. Doeff, *ACS Appl. Mater. Interfaces*, 2015, **7**, 2073–2081.

55 P. Badami, J. M. Weller, A. Wahab, G. Redhammer, L. Ladenstein, D. Rettenwander, M. Wilkening, C. K. Chan and A. N. M. Kannan, *ACS Appl. Mater. Interfaces*, 2020, **12**, 48580–48590.

56 J. T. S. Irvine, D. C. Sinclair and A. R. West, *Adv. Mater.*, 1990, **2**, 132–138.

57 W. Xia, B. Xu, H. Duan, Y. Guo, H. Kang, H. Li and H. Liu, *ACS Appl. Mater. Interfaces*, 2016, **8**, 5335–5342.

58 Y. Zhang, J. Cai, F. Chen, R. Tu, Q. Shen, X. Zhang and L. Zhang, *J. Alloys Compd.*, 2015, **644**, 793–798.

59 J. M. Weller, J. A. Whetten and C. K. Chan, *ACS Appl. Energy Mater.*, 2018, **1**, 552–556.